

Constraining the luminosity function of active galactic nuclei through the reionization observations in the SKA era

Kai T. KONO,^{1,*} Taichi TAKEUCHI,¹ Hiroyuki TASHIRO,^{1,*} Kiyotomo ICHIKI,^{1,2*†} Tsutomu T. TAKEUCHI,^{1,3*}

¹Division of Particle and Astrophysical Science, Nagoya University, Nagoya 464–8602, Japan

²Kobayashi-Maskawa Institute for the Origin of Particles and the Universe, Nagoya University, Nagoya 464–8602, Japan

³The Research Center for Statistical Machine Learning, the Institute of Statistical Mathematics, 10–3 Midori-cho, Tachikawa, Tokyo 190–8562, Japan

*E-mail: kono.kai@c.mbox.nagoya-u.ac.jp, hiroyuki.tashiro@nagoya-u.jp, ichiki.kiyotomo@c.mbox.nagoya-u.ac.jp, takeuchi.tsutomu@g.mbox.nagoya-u.ac.jp

Received (reception date); Accepted (acceptance date)

Abstract

Ultraviolet (UV) and X-ray photons from active galactic nuclei (AGNs) can ionize hydrogen in the intergalactic medium (IGM). We solve radiative transfer around AGNs in high redshift to evaluate the 21-cm line emission from the neutral hydrogen in the IGM and obtain the radial profile of the brightness temperature in the epoch of reionization. The ionization profile extends over 10 [Mpc] comoving distance which can be observed in the order of 10 [arcmin]. From estimation of the radio galaxy number counts with high sensitivity observation through the Square Kilometre Array (SKA), we investigate the capability of parameter constrains for AGN luminosity function with Fisher analysis for three evolution model through cosmic time. We find that the errors for each parameter are restricted to a few percent when AGNs are sufficiently bright at high redshifts. We also investigate the possibility of further parameter constraints with future observation beyond the era of SKA.

Key words: galaxies: evolution – galaxies: LF, mass function – quasars: supermassive black holes – radiative transfer

1 Introduction

Supermassive black holes (SMBH) are observed in the center of almost all massive galaxies (Ferrarese & Ford 2005). Their mass is often $> 10^9 M_\odot$. Many observations suggest that SMBH masses are related to the masses and/or velocity dispersions in the bulges of host galaxies (e.g., Magorrian et al. 1998; Ferrarese & Merritt 2000; Gebhardt et al. 2000; Marconi & Hunt 2003). This fact implies the co-evolution of an SMBH and a host galaxy. There are many works about the role of SMBHs

in the galaxy evolution (see, e.g., Cattaneo et al. 2009, and references therein). However, the origin of SMBHs, when and how SMBHs formed, is one of the biggest challenges in the structure formation of the Universe. High-redshift quasar (QSO) surveys revealed that SMBHs already existed at $z > 6$ (Fan et al. 2006; Mortlock et al. 2011; Wu et al. 2015). To explain the formation of the SMBHs in such high redshifts, many scenarios are proposed. Although it is widely accepted that SMBHs have evolved from a kind of seeds, various SMBH seeds are claimed, including the remnants of first stars (Madau &

Rees 2001; Alvarez et al. 2009; Whalen & Fryer 2012), the direct collapse of massive gas cloud (Loeb & Rasio 1994; Eisenstein & Loeb 1995; Begelman et al. 2006), and the primordial black holes formed in the very early universe (Bean & Magueijo 2002; Dückting 2004). Observations of SMBHs at high-redshifts are strongly desired to restrict the seed scenarios.

One of the observables to explore SMBHs in the early Universe is active galactic nuclei (AGNs). X-ray surveys are efficient to investigate the evolution and population of AGNs at high redshifts. Wide and deep X-ray surveys by XMM and Chandra provided large samples of AGNs, and consequently the abundance of AGNs in $z \sim 1\text{--}5$ is well studied (Brandt & Alexander 2015). Nonetheless, the information on AGNs in $z > 5$ is still limited. Currently, about 30 sources are found in $z > 6.5$ (Pons et al. 2020; Bañados et al. 2018; Nanni et al. 2018). Recently it is claimed that a significant population of faint AGNs would exist at $4 < z < 6.5$ (Giallongo et al. 2015). The existence of such faint AGNs would give a strong impact on the ionization process during the epoch of reionization (EoR) (Madau & Haardt 2015; Yoshiura et al. 2017; Mitra et al. 2018).

The EoR is an era at which the intergalactic medium (IGM) has drastically changed from neutral to highly ionized. Cosmological observations, including CMB, distant QSO and galaxy observations revealed that the cosmic reionization process has completed before $z \sim 6$. Cosmic reionization is driven by ionizing photons with an energy of $E > 13.6$ eV. The UV radiation from newly formed massive stars is thought to be the main source of the ionizing photons. However, AGNs are still a candidate of a significant contributor to the reionization. How much star forming galaxies and AGNs contribute to the cosmic reionization has still been actively debated (Fontanot et al. 2012; Bouwens et al. 2012). Further, since the typical UV slopes of star forming galaxies and AGN are different, the radial ionization profile around these sources are very different. Thus, it is necessary to determine the shape of luminosity function of ionizing sources at high redshifts for the determination of ionizing history of the Universe. Some literature are trying to quantify the evolution of luminosity function in the EoR (Giallongo et al. 2015; Madau & Haardt 2015; Parsa et al. 2018) to quantify cosmic reionization.

Redshifted 21-cm line observations can be expected to provide new constraints on the AGN luminosity function in high redshifts. Measurement of the 21-cm radiation from neutral hydrogen in the IGM is useful as a probe of the physical properties of the IGM reionization process in high redshifts (for a review, see Furlanetto et al. 2006).

Currently, the detection of 21 cm signals from the epoch of reionization has not been confirmed yet. The Square Kilometre Array (SKA) project is expected to measure the 21-cm signals from the epoch of reionization and even from the Cosmic Dawn (Koopmans et al. 2015). Since AGNs emit ionizing photons and ionize the IGM, AGNs can contribute to generating the spatial fluctuations of 21-cm signals (Kulkarni et al. 2017). In addition, AGNs can serve as X-ray sources. Since X-ray heats the IGM and produce Lyman- α photons which can excite the hyperfine structure of neutral hydrogen, it would also affect the 21-cm signals (Pritchard & Furlanetto 2007; Christian & Loeb 2013; Fialkov et al. 2014). The constraint on the number of X-ray sources obtained from redshifted 21-cm measurements, then, can provide useful information about the AGN population.

In this paper, we investigate the feasibility of the AGN number count by using redshifted 21-cm observations in the SKA era. Luminous objects before the epoch of reionization can make distinctive signal structures on redshifted 21-cm signal maps. Some preceding papers have been published to investigate the signal profiles of first stars, galaxies, quasars and primordial black holes (Zaroubi et al. 2007; Chen & Miralda-Escudé 2008; Tashiro & Sugiyama 2013; Yajima & Li 2014). Therefore, we can expect to find luminous objects by 21-cm surveys. Focusing on the 21-cm signal created by individual AGNs, we investigate the number count of AGNs with a simple analytic model of the luminosity function of AGNs. Then, using the number count dependence on the redshift and angular resolution, we demonstrate how well we can recover the luminosity function through the SKA observation.

This paper is organized as follows. In Section 2, we describe AGN luminosity function and galaxy evolution models we assumed. Section 3 is dedicated to calculate the 21-cm signal around an AGN to estimate the limit luminosity with the SKA sensitivity. In Section 4, we present our results in galaxy number counts and the capability of galaxy evolution parameter constraints and discuss for future observations. Finally, we conclude in Section 5.

2 AGN luminosity function (LF)

AGN activities in high redshift ($z > 8$) could provide huge impact on cosmological structure formation history, as we discussed in Section 1. However, either theoretically or observationally, the AGN luminosity function (LF) at high redshifts ($z > 8$) is totally uncertain. The aim of this paper is to investigate the feasibility of future 21-cm observation including SKA for probing the AGN LF. To demonstrate this, we introduce a simple model of the AGN LF.

	\mathcal{A}	γ_1	γ_2	β_1	β_2	L_{10*}
Model I	10^{-4}	1.5	3.5	-1.0	-0.02	0.85
Model II	$10^{-4.5}$	1.5	3.5	1.0	-0.3	0.85
Model III	10^{-5}	1.5	3.5	2.0	-0.5	0.85

Table 1. Parameter set for our DP models of the AGN LF in high redshifts.

$$\frac{dn}{d\log L} = (1+z)^{Q(z)} \frac{A}{\left(\frac{L}{L_*}\right)^{\gamma_1} + \left(\frac{L}{L_*}\right)^{\gamma_2}}, \quad (1)$$

where L_* is the critical luminosity of the power-law index, γ_1 and γ_2 ($\gamma_1 < \gamma_2$) are the power-law indices for the lower and higher luminosity sides, respectively, A is a normalizing factor at the normalized luminosity $L_n = 10^{10}$ [L_\odot], and L_* is the characteristic luminosity that determines transition of the power-law indices. In the model, $Q(z)$ represents the redshift evolution of the LF. This type of formulation has been often used for the studies on the far-infrared (FIR) galaxy evolution (e.g., Lonsdale et al. 1990; Saunders et al. 1990; Lawrence et al. 1999), and recalling the tight relation between X-ray and FIR emission, the assumption is naturally justified (e.g., David et al. 1992). We take the first order of polynomial of redshift as

$$Q(z) = \beta_1 + \beta_2 z. \quad (2)$$

where the parameters β_i are the power-law indices for the redshift dependence. Therefore, in our model, the model parameter set is $\theta = \{A, L_{10*}, \gamma_1, \gamma_2, \beta_1, \beta_2\}$, where L_{10*} is defined as $L_{10*} = L_* / L_n$. This double power-law (DP) model agrees well with the AGN observation at low redshifts, and commonly used as a proper description of the AGN LF (e.g., Mauch & Sadler 2007; Ueda et al. 2014). Therefore, we adopt this model even for a high redshift LF which we are interested in this paper.

In order to choose the fiducial parameter set of our model, it is useful to calculate the UV emissivity and compare it with high redshift AGN observation. The emissivity at the energy E_{912} corresponding to the wavelength, 912 Å, can be obtained by

$$\epsilon_{912} = \int L_E(L; E_{912}) \frac{dn}{dL} dL, \quad (3)$$

where $L_E(L; E)$ is the energy spectrum of AGNs with the total luminosity L . For simplicity, we assume that AGNs have a power-law energy spectrum with the spectral index p ,

$$L_E(L; E) = \mathcal{A}(L) \left(\frac{E}{E_{912}} \right)^p \quad (E_{912} < E < 100 \text{ keV}), \quad (4)$$

where we set $p = -1$ as suggested by Kuhlen & Madau (2005), $E_{\min} = 200$ eV and \mathcal{A} is the normalization factor which satisfies the relation $L = \int L_E(L; E) dE$ over the

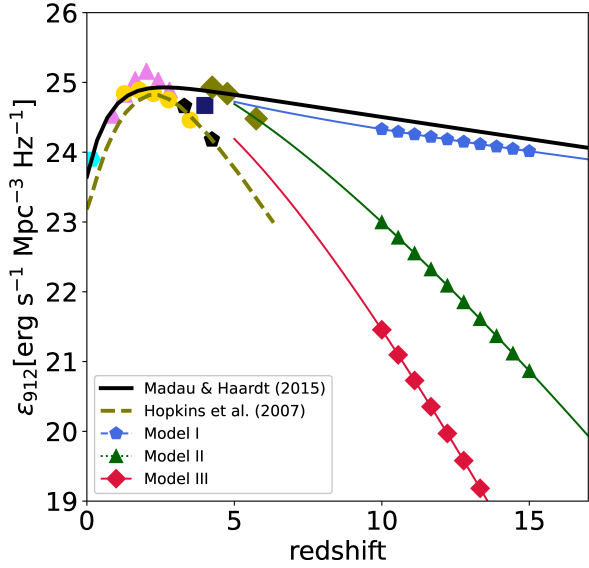


Fig. 1. The expected emissivity of ionizing photon from AGN during cosmic time (pentagons, triangles, diamonds, and solid lines) for our DP models. The black solid line and olive dashed line are empirical model of emissivity obtained by Madau & Haardt (2015) and Hopkins et al. (2007), respectively. Observations are presented for comparison as follows; cyan pentagon: Schulze et al. (2009), pink triangles: Palanque-Delabrouille et al. (2013), yellow circles: Bongiorno et al. (2007), black pentagons: Masters et al. (2012), dark blue square: (Glikman et al. 2011), olive diamonds: Giallongo et al. (2015), respectively.

integration interval $E_{912} z < E < 100$ keV.

Figure 1 presents the emissivity, ϵ_{912} , for our three fiducial parameter sets. We summarize our parameter set in table 1. Currently ϵ_{912} is measured in the redshifts lower than $z = 7$. We plot the several observation data in colored marks. The figure tells us that our fiducial models lie inside the scatter of the observation data in lower redshifts. For comparison, we plot two empirical models proposed by Madau & Haardt (2015) and Hopkins et al. (2007) in the black and olive solid lines, respectively.

In our fiducial models, Model I has the strongest emissivity. In this model, the redshift evolution is similar to the model of Madau & Haardt (2015), but they constructed it based on optically selected AGN samples. In Model III, we choose the parameters to match the redshift evolution of ϵ_{912} to the galaxy evolution model at low redshifts (Hopkins et al. 2007) which is based on multiple observations on X-ray, near- and mid-IR bands.

3 21-cm signal around an AGN

The AGNs can ionize and heat the surrounding IGM. As a result, it is expected that the unique spatial distribution

of 21 cm brightness temperature is observed around AGNs as the 21-cm signals of AGNs. The strength and size of the signal depends on the AGN luminosity. Therefore, we can count the abundance of AGNs with L through measuring the 21-cm signals by future 21-cm observation. In this section we calculate the 21-cm signal produced by AGNs with L .

3.1 IGM neutral fraction and temperature around an AGN

The evaluation of the 21-cm signal requires the spatial distribution of the neutral fraction x_{HI} and gas temperature T_{k} of hydrogen around an AGN. To obtain these distributions, we follow the method in Zaroubi et al. (2007).

As mentioned in the previous section, we assume that AGNs have the power-law energy spectrum, Eq. (4). With the assumption of the isotropic photon emission, the energy flux at distance r from an AGN can be obtained by

$$\mathcal{F}(E, r) = e^{-\tau(E, r)} \frac{L_E(E)}{4\pi r^2}. \quad (5)$$

Here $\tau(E, r)$ is the optical depth for a photon with energy E from the AGN to the distance r ,

$$\tau(E, r) = \int_0^r n_{\text{H}} x_{\text{HI}}(r) \sigma(E) dr, \quad (6)$$

where n_{H} is the IGM hydrogen number density and $x_{\text{HI}}(r)$ is the hydrogen neutral fraction at r . Taking into account the helium contribution, the cross-section $\sigma(E)$ is given by

$$\sigma(E) = \sigma_{\text{H}}(E) + \frac{n_{\text{He}}}{n_{\text{H}}} \sigma_{\text{He}}(E), \quad (7)$$

where $\sigma_{\text{H}}(E) = \sigma_0 (E_0/E)^3$ with $\sigma_0 = 6 \times 10^{-18} \text{ cm}^2$ and $E_0 = 13.6 \text{ eV}$. For the helium contribution, we set the number ratio of helium to hydrogen to $n_{\text{He}}/n_{\text{H}} = 1/12$ and take $\sigma_{\text{He}}(E)$ as Fukugita & Kawasaki (1994)

$$\sigma_{\text{He}}(E) = 1.13 \times 10^{-14} \left(\frac{1}{E^{2.05}} - \frac{9.775}{E^{3.05}} \right) [\text{cm}^2]. \quad (8)$$

Next we consider the IGM ionization by an AGN with the energy flux given by Eq. (5). In the calculation of the ionization, we simply assume that the photoionization due to the AGN is balanced by recombination. Therefore, the neutral fraction of hydrogen x_{HI} is obtained by solving the equilibrium equations between them Zaroubi & Silk (2005),

$$\alpha^{(\text{B})} n_{\text{H}}^2 (1 - x_{\text{HI}})^2 = \Gamma(r) n_{\text{H}} x_{\text{HI}} \left(1 + \frac{\sigma_{\text{He}}}{\sigma_{\text{H}}} \frac{n_{\text{He}}}{n_{\text{H}}} \right), \quad (9)$$

where $\alpha^{(\text{B})}$ is the case-B recombination rate, $\alpha^{(\text{B})} = 2.6 \times 10^{-13} T_4^{-0.85} \text{ cm}^3 \text{ s}^{-1}$ with $T_4 = T_{\text{k}}/10^4$ [K]. In Eq. (9), $\Gamma(r)$ represents the photoionization rate per a hydrogen atom at the distance r from the AGN,

$$\Gamma(r) = \int_{E_0}^{\infty} \sigma(E) \mathcal{F}(E, r) \left[1 + \frac{E}{E_0} \phi(E, x_{\text{e}}) \right] \frac{dE}{E}. \quad (10)$$

Here we introduce the function $\phi(E, x_{\text{e}})$, which provides the fraction of the energy used for the secondary ionizations over the injected energy from an AGN with $x_{\text{e}} = 1 - x_{\text{HI}}$. For $\phi(E, x_{\text{e}})$, we adopt the fitting formula in Shull & van Steenberg (1985) and Dijkstra et al. (2004),

$$\phi(E, x_{\text{e}}) = 0.39 \left[1 - x_{\text{e}}^{0.4092} a(E, x_{\text{e}}) \right]^{1.7592},$$

$$a(E, x_{\text{e}}) = \frac{2}{\pi} \arctan \left[\left(\frac{E}{0.12 \text{ keV}} \right) \left(\frac{0.03}{x_{\text{e}}^{1.5}} + 1 \right)^{0.25} \right]. \quad (11)$$

We plot the results as the radial profiles of the neutral fraction in Figure 2. In the figure, we set the AGN luminosity to $L = 10^{10} L_{\odot}$ and $10^{12} L_{\odot}$. As the luminosity increases, the ionized region becomes large. When the AGN has the Eddington luminosity with $10^7 M_{\odot}$, the ionized region expands to 10 Mpc scales. Figure 2 also shows us the redshift dependence of the ionized region. Since the ionization and recombination process depends on the number density, the ionized region is smaller in higher redshift in physical scales. Note that Figure 2 is represented in the comoving scale, and therefore the redshift dependence is not obvious.

The X-ray photons emitted from the AGN can also heat the IGM. To obtain the temperature heated by the AGN, we take two assumptions. The first assumption is that the heating rate is constant during the AGN lifetime t_{life} . The other is that the cooling effects are negligible. In the IGM, the main cooling mechanisms are the expansion of the Universe and the Compton cooling with CMB photons. Compared with the AGN lifetime, which we take $t_{\text{life}} \sim 10$ Myrs, these time scales are longer at redshifts $10 < z < 20$.

With these assumptions, the temperature at the distance r , $T_{\text{k}}(r)$, is given by

$$T_{\text{k}}(r) = \frac{2}{3} \frac{\mu \mathcal{H}(r) t_{\text{life}}}{n_{\text{H}} k_{\text{B}}}, \quad (12)$$

where μ is the mean molecular weight and k_{B} is the Boltzmann constant. In Eq. (12), $\mathcal{H}(r)$ is the heating rate per unit volume at distance r which can be written as

$$\mathcal{H}(r) = f n_{\text{H}} x_{\text{HI}}(r) \int_{E_0}^{\infty} \sigma(E) \mathcal{F}(E, r) dE, \quad (13)$$

where f represents the fraction of the photon energy which is transferred to the IGM temperature through the collisional excitation of the IGM. We used the fitting formula for f provided by Shull & van Steenberg (1985);

$$f = C [1 - (1 - x_{\text{e}}^a)^b] \quad (14)$$

with $C = 0.9771$, $a = 0.2663$, $b = 1.3163$, imposing the lower limit as $f = 0.11$ for $x < 10^{-4}$ as modified in Zaroubi

et al. (2007). As the distance r increases, the heating efficiency becomes low. At a sufficient distance, the temperature should correspond to the background baryon temperature $\bar{T}_k(z)$. Therefore, if $T_k(r)$ in Eq. (12) becomes lower than the background baryon temperature at r_* , we set $T_k(r) = \bar{T}_k(z)$ at $r > r_*$.

We plot the kinetic temperature radial profile around an AGN in Figure 3. Similarly to the case of the ionization, as the luminosity increases, the AGN can heat up neutral hydrogen in the IGM at further distance. In particular, AGNs with $L = 10^{12} L_\odot$ can heat the IGM even at comoving 100 Mpc distance. In the inner side which is highly ionized, the temperature does not depend on the distance and the AGN luminosity. This is because the heating rate, Eq. (13), is almost constant with the equilibrium assumption in Eq. (9) in the highly ionized region, $x_{\text{HI}} \ll 1$. In other words, once the region is highly ionized, there happens no additional heating any more and the temperature gets saturated. Figure 3 also tells us the redshift dependence of the temperature. The heating rate grows as the redshift increases. Therefore, the resultant heated temperature is also large in high redshifts.

3.2 Different brightness temperature

In observations of redshifted 21-cm signals, the observed value is described as the difference of the brightness temperature at the observed frequencies from the CMB temperature. This different brightness temperature is given by (Madau et al. 1997; Ciardi & Madau 2003)

$$\delta T_b \equiv T_b - T_{\text{CMB}}(z) = \frac{[T_s - T_{\text{CMB}}(z)](1 - e^{-\tau})}{1 + z}, \quad (15)$$

where T_{CMB} , T_b and T_s represent the CMB temperature, the 21-cm brightness temperature and its spin temperature, respectively. In the equation, τ is the 21-cm optical depth of the IGM,

$$\tau = \frac{3}{4} \frac{h_P c^3 A_{10}}{8\pi \nu_{10}^2 k_B} \frac{x_{\text{HI}} n_{\text{H}}}{T_s H(z)}, \quad (16)$$

where A_{10} is the Einstein A-coefficient for the transition, ν_{10} is the frequency corresponding to the energy difference between the transition states, h_P is the Planck constant and c is the speed of light. In Eq. (15), we ignore the effects of the peculiar velocity and the thermal velocity of the gas on the velocity gradient along the line-of-sight, which are generally smaller than the Hubble expansion effect considered in Eq. (16).

Since we are interested in the 21-cm signal from the IGM, the optically thin limit, $\tau \ll 1$, is valid. Therefore, we can approximate the different brightness temperature as

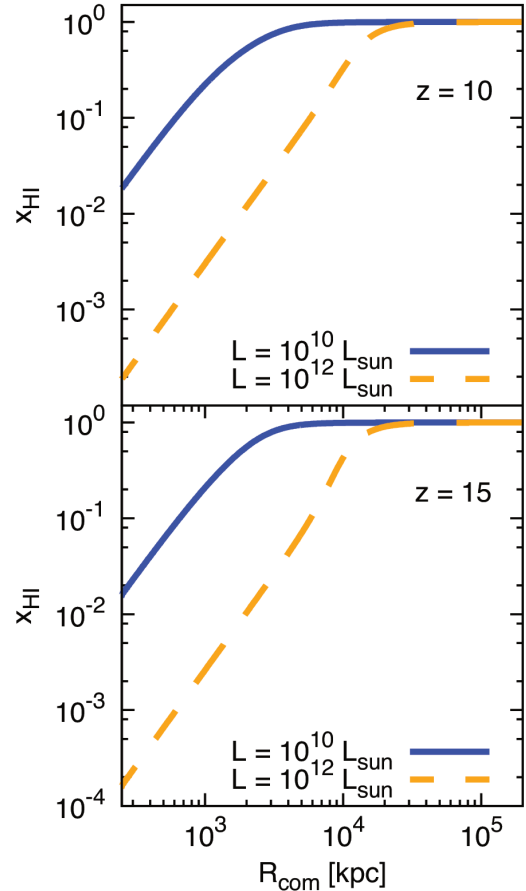


Fig. 2. The radial profile of neutral fraction around an AGN. The blue and orange lines are for $L = 10^{10} L_\odot$ and $L = 10^{12} L_\odot$, respectively. We set $z = 10$ and 12 in the top and bottom panels, respectively.

$$\delta T_b \simeq \frac{3}{32\pi} \frac{h_P c^3 A_{10}}{k_B \nu_{10}^2} \frac{x_{\text{HI}} n_{\text{H}}}{(1+z) H(z)} \left[1 - \frac{T_{\text{CMB}}(z)}{T_s} \right]. \quad (17)$$

The spin temperature of the 21-cm lines in the cosmological context is given by (Wouthuysen 1952; Field 1958)

$$T_s = \frac{T_{\text{CMB}} + y_k T_k + y_\alpha T_k}{1 + y_k + y_\alpha}, \quad (18)$$

where y_k and y_α are the kinetic coupling and Ly α coupling coefficients, respectively.

The contributions to y_k are divided into three collision terms of neutral hydrogen with neutral hydrogen, electrons and protons as

$$y_k = \frac{T_*}{A_{10} T_k} (C_H + C_e + C_p), \quad (19)$$

where C_H , C_e and C_p are the collisional de-excitation rates due to neutral hydrogen, electrons and protons and T_* is the temperature corresponds to the energy difference between singlet and triplet of electron, namely $T_* = 0.0681$ [K]. For these rates, we adopt the fitting formulae given by Kuhlen et al. (2006),

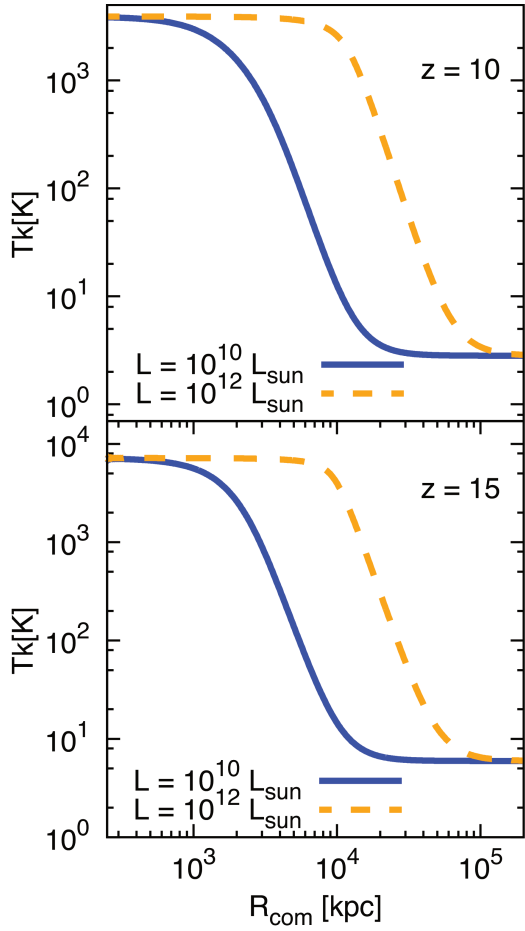


Fig. 3. The radial profile of kinetic temperature around an AGN. The colored lines are same as in Figure 2.

$$C_H = 3.1 \times 10^{-11} n_H T_k^{0.357} \exp\left(-\frac{32}{T_k}\right), \quad (20)$$

$$C_e = n_e \gamma_e, \quad (21)$$

$$C_p = 3.2 C_H \frac{n_p}{n_H}, \quad (22)$$

where γ_e represents the de-excitation coefficient for e-H collision, which is fitted with the temperature T_k by

$$\log_{10} \left(\frac{\gamma_e}{1 \text{ [cm}^3 \text{s}^{-1}]} \right) = -9.067 + 0.5 \log_{10} T_k \exp \left[-\frac{(\log_{10} T_k)^{4.5}}{1800} \right]. \quad (23)$$

The Lyman- α coupling coefficient is provided in Field (1958)

$$y_\alpha = \frac{16\pi^2 T_* e^2 f_{12} J_0(r)}{27 A_{10} T_k m_e c}, \quad (24)$$

where f_{12} is the oscillator strength of the Lyman- α transition, $f_{12} = 0.416$, and $J_0(r)$ represents the Lyman- α intensity at distance r from the AGN. To obtain $J_0(r)$, we consider the secondary collisional excitation by electrons released in the photoionization by the AGN. In this case,

the Lyman- α intensity can be written as (Zaroubi et al. 2007)

$$J_0(r) = \frac{\phi_\alpha c}{4\pi H(z)\nu_\alpha} n_H x_{\text{HI}}(r) \int_{E_0}^{\infty} \sigma(E) \mathcal{F}(E, r) dE, \quad (25)$$

where ν_α is the Lyman- α frequency and ϕ_α is the energy fraction for the secondary excitation. We set $\phi_\alpha = 0.48 \times (1 - x_e^{0.27})^{1.52}$, according to Shull & van Steenberg (1985).

Figure 4 represents the spin temperature profile around an AGN. As shown in Eq. (24), the Lyman- α coupling is proportional to x_{HI} . Therefore, in the ionized region, y_α is not effective. As a result, the spin temperature is controlled by y_k . Since the kinetic temperature is constant in the ionized region, the resultant spin temperature also keeps constant. As x_{HI} increases, y_α becomes larger than y_k and has an important role to determine the spin temperature. The Lyman- α intensity is stronger where x_{HI} is close to a unity, and the spin temperature reaches the maximum value. Moreover, the maximum value of the spin temperature is not sensitive to the AGN luminosity. This fact means that J_0 at the peak position of the spin temperature is independent of the AGN luminosity. This reason is same as in the discussion about the independence of the maximum gas temperature on the AGN luminosity. The Lyman- α photon production has been saturated at the peak position and, as a result, does not depend on the AGN luminosity. For the further discussion we refer the reader to Zaroubi et al. (2007).

Even at the cosmological distance from the AGN, the Lyman- α coupling can deviate the spin temperature from the CMB temperature. When the AGN luminosity is enough large as the Eddington luminosity with $L > 10^{12} L_\odot$, the spin temperature is well deviate even at the comoving distance larger than 10 Mpc. Since the IGM is cooler than the CMB, the spin temperature is lower than the CMB temperature in this range. At a larger distance, the spin temperature finally approaches the CMB temperature.

In Figure 4, we also show the redshift dependence of the spin temperature. Since the coupling coefficients, y_k and y_α , are proportional to the IGM hydrogen density n_H , they becomes large when the redshift increases. Additionally, the gas temperature is also large in high redshifts. Therefore, the resultant spin temperature is larger in high redshifts. The maximum value of the spin temperature at $z = 15$ is almost two times higher than at $z = 10$.

Based on the spin temperature profiles in Figure 4, we can calculate the differential brightness temperature around the AGN through Eq. (15) and (16). We plot the results in Figure 5. The region close to the AGN is ionized and the 21-cm signal vanishes there. Then gradually the

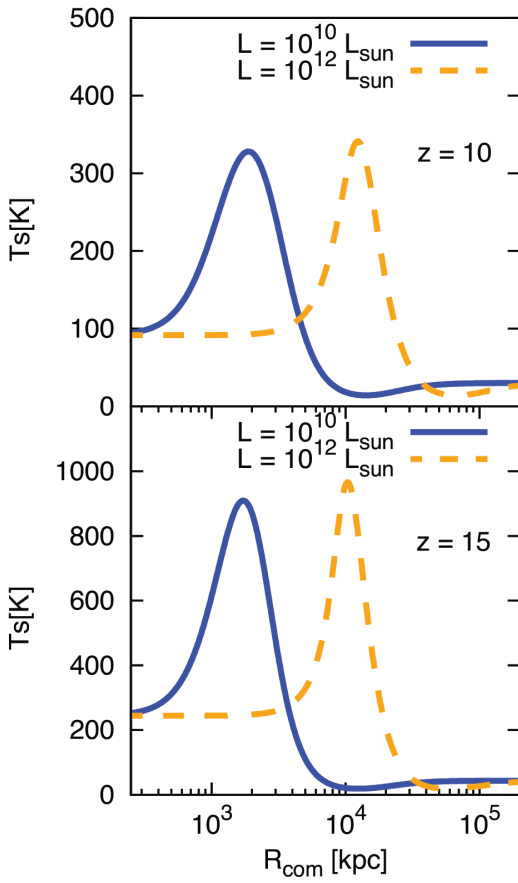


Fig. 4. The radial profile of spin temperature T_s around an AGN. The colored lines are same as in Figure 2.

positive (emission) signal arises where the gas temperature is much higher than the CMB temperature. At the sufficient distance, the signal becomes negative (absorption) and reaches the negative peak.

As shown in Eq. (17), when the spin temperature is larger than the CMB temperature (i.e., the emission signal case), the signal amplitude is saturated. However, the smaller the spin temperature, the larger the amplitude of the absorption signal is. Additionally, the absorption signal region has larger volume than the emission signal region. Therefore, the detection of the absorption signal can be easier than the detection of the emission signal.

The peak amplitude in both negative and positive sides is almost independent of the AGN luminosity, because of the same reason as in the cases of the gas temperature and spin temperature. On the contrary, the peak position depends on the AGN luminosity. Therefore, measuring the distance of the negative peak from the AGN (or the size of the negative signal region) provides with an important information to know the luminosity of the AGN at the center of the signal region.

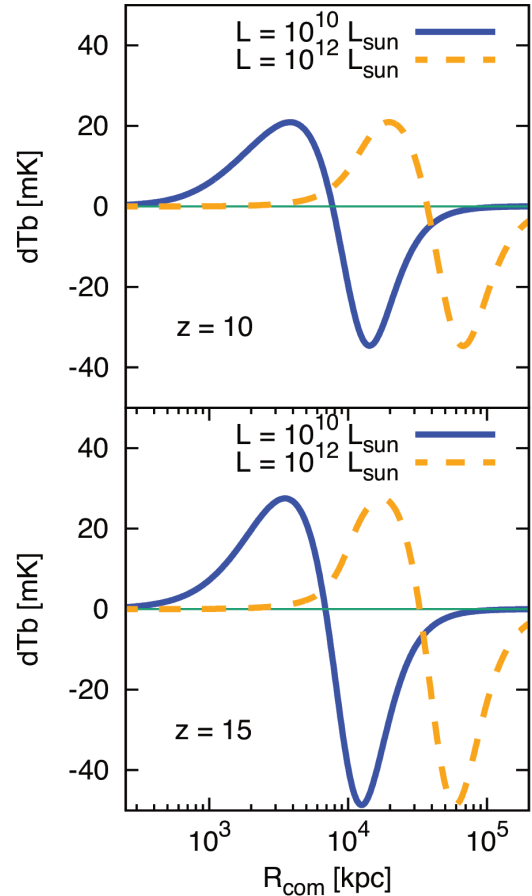


Fig. 5. The radial profile of brightness temperature δT_b around an AGN. The colored lines are same as in Figure 2.

4 AGN number count

Now we present whether future 21-cm observation, such as SKA, can access the AGN LF in high redshifts to demonstrate the AGN number count with our three fiducial models. First, we evaluate the detectability of the 21-cm AGN signals obtained in the previous section with considering the current design of the SKA observation. Then to investigate the possible constraint on the LF, we conduct a Fisher matrix analysis for our fiducial models.

4.1 Detectability of the AGN signals by SKA

To evaluate the signal detected by SKA, we need to take into account the finite resolutions of the observation in the frequency (the line-of-sight direction) and the angular direction (the direction perpendicular to the line-of-sight direction). We can obtain the predicted signal for the observation by smoothing the signal profile with these resolutions.

First, we make the 3-dimensional signal map from the radial profile of the different brightness temperature, as

suming the spherical symmetry. For smoothing, we consider the cylindrical volume. The width of the cylinder matches to the angular resolution $\Delta\theta$ and the length corresponds to the spatial resolution in the line-of-sight direction determined by the frequency resolution $\Delta\nu$. To obtain the smoothed 21-cm signal δT_b which is defined in eq. (17) around the AGN, we smooth the signal with the cylindrical volume at whose center the AGN locates.

To discuss the detectability by SKA, we compare the signal $|\delta T_b|$ with the noise level of the SKA observation. The noise of an interferometer for an observation wavelength λ_{obs} is written in terms of the brightness temperature as (Furlanetto et al. 2006)

$$\begin{aligned} \delta T_N(\lambda_{\text{obs}}) &= \frac{\lambda_{\text{obs}}^2}{\Delta\theta^2 A_{\text{eff}}} \frac{T_{\text{sys}}}{\sqrt{\Delta\nu t_{\text{obs}}}} \\ &\simeq 20 \text{ [mK]} \left(\frac{A_{\text{eff}}}{10^4 \text{ [m}^2\text{]}} \right)^{-1} \left(\frac{\Delta\theta}{10'} \right)^{-2} \left(\frac{1+z}{10} \right)^4 \\ &\quad \times \left(\frac{\Delta\nu}{1 \text{ [MHz]}} \frac{t_{\text{int}}}{100 \text{ [hr]}} \right)^{-1/2}, \end{aligned} \quad (26)$$

where $\Delta\theta$ is the angular resolution, $\Delta\nu$ is the frequency resolution, A_{eff} is the effective collecting area, T_{sys} is the system temperature of the observation and t_{obs} is the total observation time. In order to obtain the second line of the equation, we use $\lambda_{\text{obs}} = 21 \text{ [cm]}(1+z)$. For the SKA observation, we set $A_{\text{eff}} = 10^4 \text{ [m}^2\text{]}$ and $t_{\text{obs}} = 1000 \text{ [hours]}$. One of main contributions to T_{sys} is the synchrotron radiation in the Milky Way. Therefore, for T_{sys} , we adopt the sky temperature at high Galactic latitude,

$$T_{\text{sys}} = 180 \left(\frac{\nu_{\text{obs}}}{180 \text{ [MHz]}} \right)^{-2.6} \text{ [K]} \quad (27)$$

where ν_{obs} is the frequency corresponding to λ_{obs} .

We set our criterion for the detection to $|\delta T_b|/\delta T_N > 3$. Since $|\delta T_b|$ becomes large with increasing L of the AGN, the detection criterion can be represented as the minimum AGN luminosity for the detection, L_{min} . Figure 6 shows the redshift dependence of L_{min} for different angular resolutions, $\Delta\theta$. The noise has a strong redshift dependence coming from

$$\lambda_{\text{obs}}^2 T_{\text{sys}} \propto (1+z)^{4.6}. \quad (28)$$

Consequently, L_{min} monotonically grows in high redshifts. When the angular resolution becomes large, the noise decreases according to Eq. (26). However the smoothing volume also increases. Accordingly, the signal is diluted by the smoothing and a large luminosity is required for the detection with a large angular resolution.

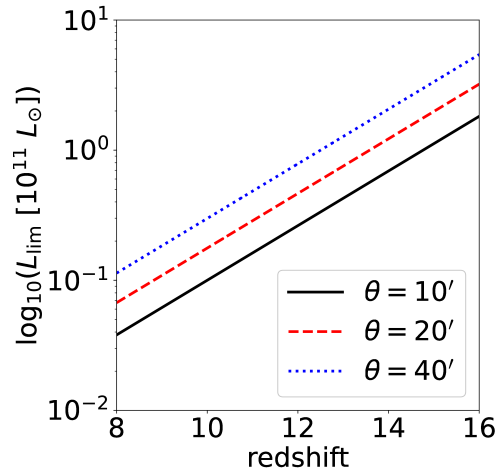


Fig. 6. The minimum luminosity for a set of $\Delta\theta$ as a function of redshift obtained from 2D convolution of 21 cm signal from AGN.

4.2 Fisher matrix analysis

Now we consider the galaxy number counts of AGNs expected to be detected by SKA. Suppose that we perform the 21 cm observation in some redshift range. We divide the redshift into some redshift bins and count the number of detected AGNs in each redshift bin. Besides, conducting the data analysis with different angular resolution (or using different range of k -modes for the image reconstruction?), we also count the detected AGN number for each configuration of the angular resolution. Therefore, we can obtain the number count in two dimensional bins for the redshift and angular resolution.

When we model the AGN LF, we can evaluate the expected number counts of AGNs whose luminosities are larger than L_{min} $N_{i,j}$, from

$$N_{i,j} = 4\pi f_{\text{sky}} \int_{z_{i,\text{min}}}^{z_{i,\text{max}}} dz \int_{L_{\text{min},j}}^{\infty} \frac{R^2(z)}{H(z)} \frac{dn}{dL} dL, \quad (29)$$

where $R(z)$ is the comoving distance to the redshift z , $z_{i,\text{min}}$ and $z_{i,\text{max}}$ are the minimum and maximum redshifts in the i -th redshift bin, f_{sky} is the sky fraction of the observation. Since SKA will have 5×5 square degree field of view, we set f_{sky} to be $f_{\text{sky}} = 0.0006$. In the equation, as shown in the previous section, L_{min} is a function of the redshift z and the angular resolution $\Delta\theta_j$ related to the j -th bin of the angular resolution.

The number count depends on the redshift and angular resolution. Therefore, we conduct the Fisher matrix analysis for our three fiducial DP models, considering the number count for several redshift bins with different angular resolution set, $\{\Delta\theta_i\}$. Fixing the angular resolution, we

can probe the redshift evolution of the AGN LF, in particular, β_1 and β_2 . On the other hand, in a fixed redshift, the number counts on different angular resolution is expected to provide the luminosity dependence of the LF, α and L_* .

We take the assumption that the likelihood distribution for the parameters is a multivariate Gaussian and takes the maximum value at the fiducial parameters. Therefore, the Fisher matrix is given by

$$F_{\mu\nu} = \sum_{i,j} \frac{1}{\sigma_{i,j}^2} \left(\frac{\partial N_{i,j}}{\partial \theta_\mu} \frac{\partial N_{i,j}}{\partial \theta_\nu} \right) \quad (30)$$

where $N_{i,j}$ is the number of the detected AGNs in the i -th bin of the observed redshifts with the j -th angular resolution. In the equation, $\sigma_{i,j}$ is the variance of $N_{i,j}$ and set to $\sigma_{i,j}^{-2} = N_{i,j}$, because we assume that the detected number in the each bin follows the Poisson statistics.

In this paper we take the ranges of z in [10, 15] and $\Delta\theta$ in [5, 40] in the unit of the arc minutes. Dividing both z and $\Delta\theta$ into 10 and 20 bins, we conduct the Fisher matrix analysis on our three fiducial models. In Figure 7, we show the $1-\sigma$ error elliptical for 10 (outside blue) and 20 (inside red) bins for the LF parameter set for Model I. As is shown in the Figure 7, the obtained errors are quite small. In particular, the errors of $\{\gamma_1, \beta_2, \log L_*\}$ are in a few percentage levels. On the other hand the errors of $\{A, \gamma_2, \beta_1\}$ are relatively large, compared with constraints on other parameters. However, as we can see later, SKA can determine these parameters in a factor level for Model I

Figure 7 also shows that there exist some strong correlations in the parameter sets. These correlation appears in order to compensate the increment (decrements) due to a parameter by other parameters. For example, when we increase β_1 , the AGN LF does not suppress on high redshifts. Therefore, to compensate it, small A or large negative β_2 is preferred.

We summarize the $1-\sigma$ errors for all our fiducial models in Table 2. When we take the low LF model (Model III), the error becomes large since the number of observable galaxy significantly decreases. We found that the strong correlations shown in Figure 7 also arises in the Model II and III. Figure 8 tells us the impact of these errors on the determination of the LF in terms of the emissivity. Here the colored shaded regions represent $1-\sigma$ error for each fiducial model. One can see that, when AGN luminosity distribution is given in the high LF model (Model I), SKA can reconstruct the LF. However, for Model 2, the reconstruction becomes worse, in particular, in high redshifts.

For simplicity, we assume that the AGN number count for each bin of the redshift and angular resolution is independent each other. Therefore, the errors of the LF parameters depends on the number of the bins. As we decrease

the bin numbers, the error becomes large. For example, if we take 10 bins for the redshift and the angular resolution, the error region increase two time larger than in Figure 8 and, as a result, we cannot determine the LF parameters even for the Model II.

At the last of this section, we discuss the impact of the observation noise on the reconstruction of the AGN function. In order to evaluate this impact, we consider an observation which has sensitivity enough to detect 10 times lower luminosity AGNs than for SKA I. We plot the result of the reconstruction in Figure 9. For Model II in high redshifts we can see the improvement for the reconstruction. However, since the SKA I sensitivity is enough to measure the number counts for Model I and Model II in low redshifts, the reconstruction is not improved even for the better sensitivity. Besides, it is impossible to obtain reasonable constraints on the parameters of Model III even in the better sensitivity.

5 Summary

AGNs can heat up the surrounding IGM gas by their UV and X-ray emission. Before the epoch of reionization, the heated neutral IGM can create the observable 21-cm emissions. Therefore, AGNs in high redshifts are promising targets in future redshifted 21-cm observations. In this paper we have investigated the AGN number count by future 21-cm observation as a probe of the AGN LF in high redshifts.

First we have evaluated the 21-cm signals of AGNs before the epoch of reionization. Assuming the power-law spectrum of the AGN UV and X-ray emission, we have calculated the radial profile of the IGM ionization fraction and temperature around an AGN by solving the radiative transfer of the AGN emission. We have shown that AGNs can heat up the IGM gas even at the cosmological distance, i.e., comoving 10 Mpc, depending on the luminosity of AGNs. As a result, AGNs can create the 21-cm signals whose angular size is roughly in the order of 10 arc-minutes.

The minimum amplitude of the 21 cm signal for the detection depends on the redshift and the angular resolution of observations. Therefore measuring the dependence of the AGN number count on the redshift and angular resolution allow us to probe the LF of AGNs. To demonstrate the LF by AGN number count we propose the simple analytic form of the LF with several parameters which can recover well the emissivity of two typical empirical models, Madau & Haardt (2015) and Hopkins et al. (2007).

Considering the 21-cm observations by SKA in the redshift range from $z = 15$ to $z = 10$ with the arc-minutes

	$\delta \log \mathcal{A}$	$\delta \gamma_1$	$\delta \gamma_2$	$\delta \beta_1$	$\delta \beta_2$	$\delta \log L_*$
Model I	0.22	7.3×10^{-2}	3.0×10^{-2}	2.6×10^{-1}	6.1×10^{-3}	0.030
Model II	2.3	4.5×10^{-1}	1.8×10^{-1}	2.9	7.2×10^{-2}	0.18
Model III	25	3.1	1.1	3.1×10^1	1.2	0.81

Table 2. 1σ errors for model parameters for (20×20) -bin configurations in our AGN model.

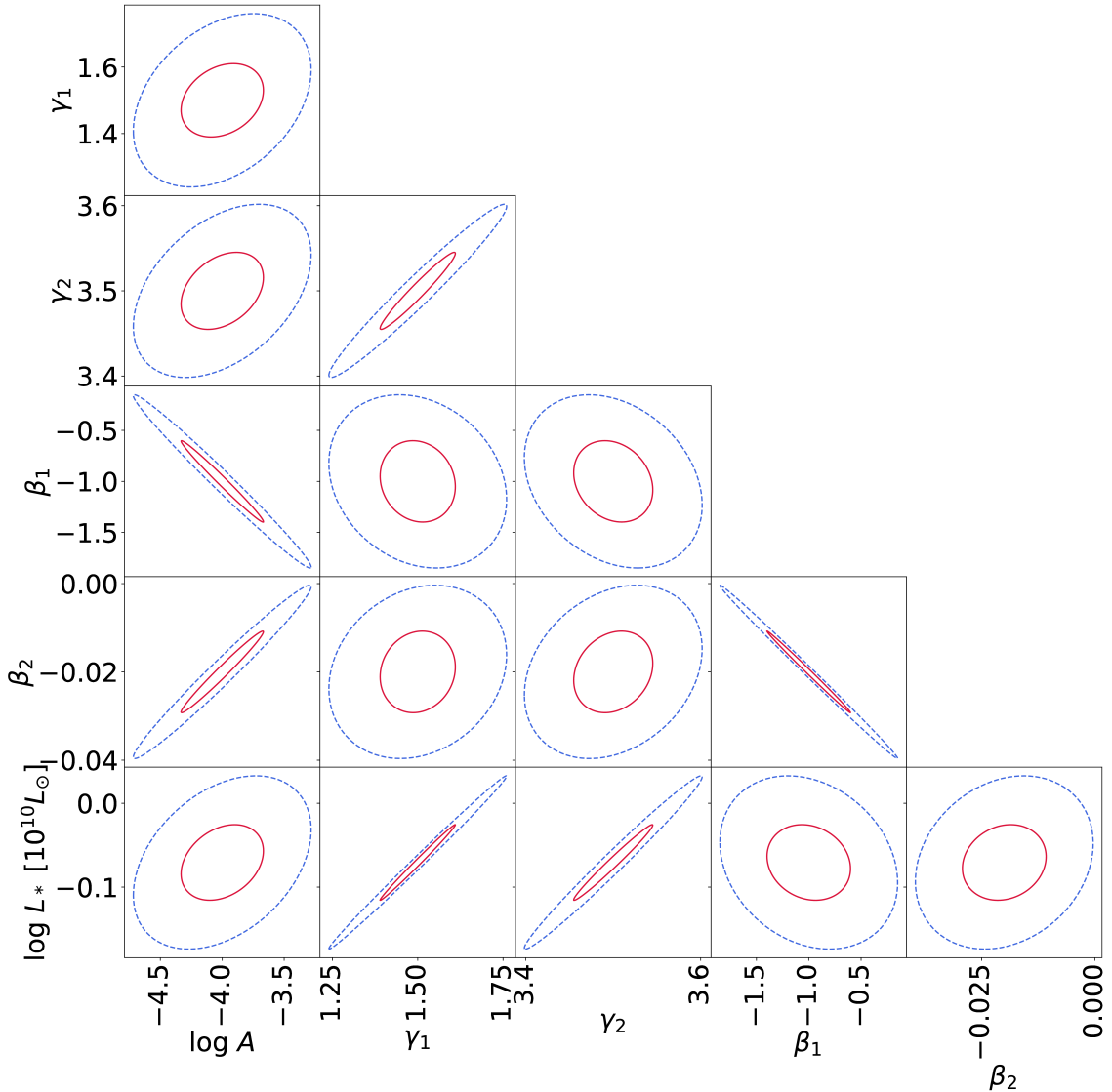


Fig. 7. The result of parameter constraint with Fisher analysis. The redshift and array configuration are divided into 10 bins for outer dashed elliptical and 20 bins for inner solid elliptical.

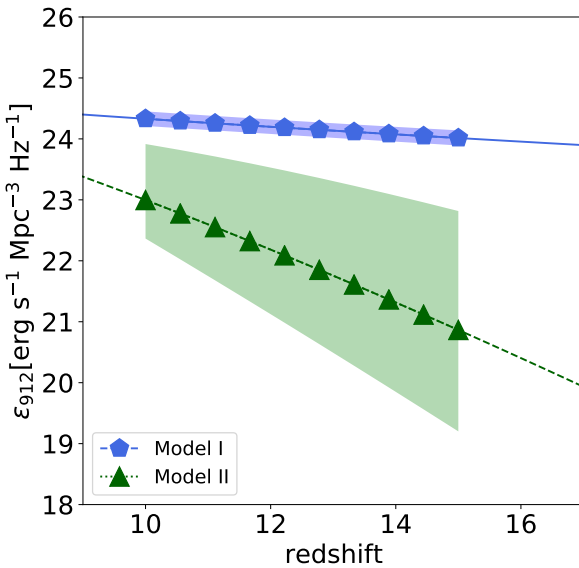


Fig. 8. The expected emissivity and estimated errors for 20×20 configurations. The colored is derived by considering $1-\sigma$ error for the AGN LF parameters.

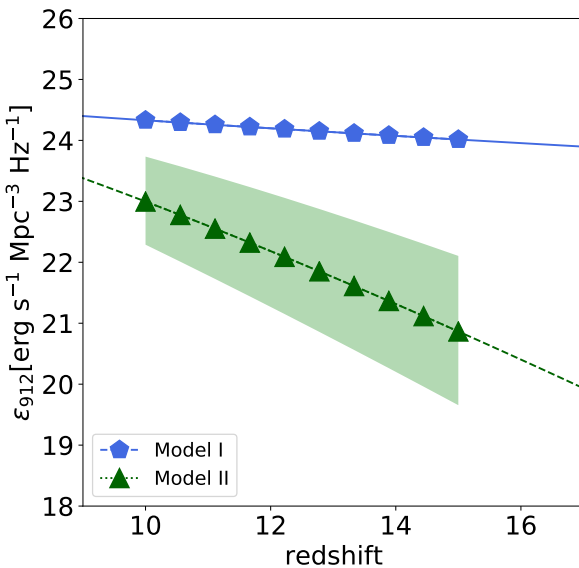


Fig. 9. Bins of galaxy number counts are divided into 20×20 observational configurations but flux limit is assumed to be $L_{\text{lim}} = 1/10 L_{\text{lim},0}$.

angular resolution, we perform the Fisher matrix analysis to investigate how AGN number count can recover the LF. We have found that SKA can probe the LF which is similar to the one suggested by Madau & Haardt (2015). However for the type proposed by Hopkins et al. (2007), which is three order of magnitude smaller than the one by Madau & Haardt (2015) in the emissivity, it is difficult for SKA to determine the LF parameters.

Acknowledgments

This work has been supported by JSPS (Grant numbers: JPJSCCA20200002, 17H0110, 18K03616, and 19H05076) and JST AIP Acceleration Research Grant Number JP20317829. This work has also been supported in part by the Sumitomo Foundation Fiscal 2018 Grant for Basic Science Research Projects (180923), and the Collaboration Funding of the Institute of Statistical Mathematics “New Development of the Studies on Galaxy Evolution with a Method of Data Science”.

References

Alvarez, M. A., Wise, J. H., & Abel, T. 2009, *ApJ*, 701, L133
 Bañados, E., Connor, T., Stern, D., et al. 2018, *ApJ*, 856, L25
 Bean, R., & Magueijo, J. 2002, *Phys. Rev. D*, 66, 063505
 Begelman, M. C., Volonteri, M., & Rees, M. J. 2006, *MNRAS*, 370, 289
 Bongiorno, A., Zamorani, G., Gavignaud, I., et al. 2007, *A&A*, 472, 443
 Bouwens, R. J., Illingworth, G. D., Oesch, P. A., et al. 2012, *ApJL*, 752, L5
 Brandt, W. N., & Alexander, D. M. 2015, *A&AR*, 23, 1
 Cattaneo, A., Faber, S. M., Binney, J., et al. 2009, *Nature*, 460, 213
 Chen, X., & Miralda-Escudé, J. 2008, *ApJ*, 684, 18
 Christian, P., & Loeb, A. 2013, *Journal of Cosmology and Astroparticle Physics*, 2013, 014
 Ciardi, B., & Madau, P. 2003, *ApJ*, 596, 1
 David, L. P., Jones, C., & Forman, W. 1992, *ApJ*, 388, 82
 Dijkstra, M., Haiman, Z., & Loeb, A. 2004, *ApJ*, 613, 646
 Düchting, N. 2004, *Phys. Rev. D*, 70, 064015
 Eisenstein, D. J., & Loeb, A. 1995, *ApJ*, 443, 11
 Fan, X., Strauss, M. A., Richards, G. T., et al. 2006, *AJ*, 131, 1203
 Ferrarese, L., & Ford, H. 2005, *Space Sci. Rev.*, 116, 523
 Ferrarese, L., & Merritt, D. 2000, *ApJ*, 539, L9
 Fialkov, A., Barkana, R., & Visbal, E. 2014, *Nature*, 506, 197
 Field, G. B. 1958, *Proceedings of the IRE*, 46, 240
 Fontanot, F., Cristiani, S., & Vanzella, E. 2012, *MNRAS*, 425, 1413
 Fukugita, M., & Kawasaki, M. 1994, *MNRAS*, 269, 563
 Furlanetto, S. R., Oh, S. P., & Briggs, F. H. 2006, *Phys. Rep.*, 433, 181
 Gebhardt, K., Bender, R., Bower, G., et al. 2000, *ApJ*, 539, L13
 Giallongo, E., Grazian, A., Fiore, F., et al. 2015, *A&A*, 578, A83

Glikman, E., Djorgovski, S. G., Stern, D., et al. 2011, *ApJ*, 728, L26

Hopkins, P. F., Richards, G. T., & Hernquist, L. 2007, *ApJ*, 654, 731

Koopmans, L., Pritchard, J., Mellema, G., et al. 2015, in *Advancing Astrophysics with the Square Kilometre Array (AASKA14)*, 1

Kuhlen, M., & Madau, P. 2005, *MNRAS*, 363, 1069

Kuhlen, M., Madau, P., & Montgomery, R. 2006, *ApJ*, 637, L1

Kulkarni, G., Choudhury, T. R., Puchwein, E., & Haehnelt, M. G. 2017, *MNRAS*, 469, 4283

Lawrence, A., Rowan-Robinson, M., Ellis, R. S., et al. 1999, *MNRAS*, 308, 897

Loeb, A., & Rasio, F. A. 1994, *ApJ*, 432, 52

Lonsdale, C. J., Hacking, P. B., Conrow, T. P., & Rowan-Robinson, M. 1990, *ApJ*, 358, 60

Madau, P., & Haardt, F. 2015, *ApJ*, 813, L8

Madau, P., Meiksin, A., & Rees, M. J. 1997, *ApJ*, 475, 429

Madau, P., & Rees, M. J. 2001, *ApJ*, 551, L27

Magorrian, J., Tremaine, S., Richstone, D., et al. 1998, *AJ*, 115, 2285

Marconi, A., & Hunt, L. K. 2003, *ApJ*, 589, L21

Masters, D., Capak, P., Salvato, M., et al. 2012, *ApJ*, 755, 169

Mauch, T., & Sadler, E. M. 2007, *MNRAS*, 375, 931

Mitra, S., Choudhury, T. R., & Ferrara, A. 2018, *MNRAS*, 473, 1416

Mortlock, D. J., Warren, S. J., Venemans, B. P., et al. 2011, *Nature*, 474, 616

Nanni, R., Gilli, R., Vignali, C., et al. 2018, *A&A*, 614, A121

Palanque-Delabrouille, N., Magneville, C., Yèche, C., et al. 2013, *A&A*, 551, A29

Parsa, S., Dunlop, J. S., & McLure, R. J. 2018, *MNRAS*, 474, 2904

Pons, E., McMahon, R. G., Banerji, M., & Reed, S. L. 2020, *MNRAS*, 491, 3884

Pritchard, J. R., & Furlanetto, S. R. 2007, *MNRAS*, 376, 1680

Saunders, W., Rowan-Robinson, M., Lawrence, A., et al. 1990, *MNRAS*, 242, 318

Schulze, A., Wisotzki, L., & Husemann, B. 2009, *A&A*, 507, 781

Shull, J. M., & van Steenberg, M. E. 1985, *ApJ*, 298, 268

Tashiro, H., & Sugiyama, N. 2013, *MNRAS*, 435, 3001

Ueda, Y., Akiyama, M., Hasinger, G., Miyaji, T., & Watson, M. G. 2014, *ApJ*, 786, 104

Whalen, D. J., & Fryer, C. L. 2012, *ApJ*, 756, L19

Wouthuysen, S. A. 1952, *AJ*, 57, 31

Wu, X.-B., Wang, F., Fan, X., et al. 2015, *Nature*, 518, 512

Yajima, H., & Li, Y. 2014, *MNRAS*, 445, 3674

Yoshiura, S., Hasegawa, K., Ichiki, K., et al. 2017, *MNRAS*, 471, 3713

Zaroubi, S., & Silk, J. 2005, *MNRAS*, 360, L64

Zaroubi, S., Thomas, R. M., Sugiyama, N., & Silk, J. 2007, *MNRAS*, 375, 1269